Chalcogenide Letters Vol. 21, No. 3, March 2024, p. 263 - 274

# Preparation and characterization of ZnO@$MoS_2$ nanocomposites: investigating photoelectrical, electrocatalytic, and electrochemical behaviors

J. M. Shi*, H. F. Zhang, H. C. Wang
*Basic Department, Yellow River Conservancy Technical Institute, KaiFeng, 475004 China*

This study presents the synthesis and characterization of 3D ZnO@$MoS_2$ nanocomposites, demonstrating their superior performance in photoelectrochemical applications. Employing a combination of hydrothermal and solvothermal methods, the research focuses on creating heterostructures with optimized interfacial characteristics. The ZnO@$MoS_2$ composites show a substantial increase in photocurrent density (1.02 mA/cm²), compared to ZnO nanorods (0.32 mA/cm²), underlining enhanced charge separation efficiency. In electrocatalytic hydrogen evolution, the heterostructures exhibit a lower onset potential (-175 mV vs RHE) and reduced Tafel slope (51 mV/dec), indicating improved catalytic activity over $MoS_2$ nanosheets. Additionally, the composites demonstrate a significant increase in electrochemical capacitance (398 F/g at 10 mV/s), suggesting potential applications in energy storage. These results highlight the efficacy of ZnO@$MoS_2$ nanocomposites in enhancing solar energy conversion and storage, providing insights into the development of next-generation semiconductor materials.

(Received December 15, 2023; Accepted March 13, 2024)

*Keywords:* Heterostructures, Photocurrent density, Hydrogen evolution reaction, Electrochemical capacitance, Nanocomposite synthesis

## 1. Introduction

In recent years, semiconductor nanocomposites have emerged as a new class of functional materials with a wide range of promising applications in electronics, photonics, sensing, energy conversion and storage [1,2]. Among various nanostructured composites, metal oxide-based systems incorporating two-dimensional (2D) transition metal dichalcogenides (TMDs) components are of particular interest due to their unique optical, electrical and catalytic properties [3,4]. Specifically, nanocomposites composed of zinc oxide (ZnO) and molybdenum disulfide ($MoS_2$) have attracted tremendous attention for renewable energy applications including photocatalysis, photoelectrochemical water splitting, and electrocatalytic hydrogen production [5].

ZnO is a II-VI group n-type semiconductor possessing a wide direct bandgap (~3.3 eV), large exciton binding energy (60 meV), excellent electron mobility, and high optical gain. These characteristics make ZnO an ideal candidate for optoelectronic applications [6]. However, the intrinsic drawbacks of ZnO such as limited visible light absorption, low hole mobility, and rapid electron-hole recombination impede its practical applications [7]. On the other hand, layered $MoS_2$ is a 2D TMD material composed of stacked S-Mo-S monolayers connected through van der Waals interactions [8]. $MoS_2$ has emerged as a promising photocatalyst and electrocatalyst owing to its chemically stable layered structure, suitable bandgap, abundant surface sites, and excellent charge transport properties [9]. Moreover, 2D $MoS_2$ nanosheets demonstrate layer-dependent tunable band structures and phase-controlled metallic to semiconducting transition [10]. By combining ZnO and $MoS_2$ to form nanoscale heterostructures, the drawbacks of the individual components can be effectively mitigated through synergistic effects while leveraging their merits [11]. Specifically, forming heterojunctions between ZnO and $MoS_2$ facilitates spatial charge separation and interfacial charge transfer, expands the photoresponse range, provides more catalytic active sites, and enables optimized band alignments.

* Corresponding author: sjm8380@163.com
https://doi.org/10.15251/CL.2024.213.263

Extensive efforts have been dedicated to synthesizing ZnO-$MoS_2$ nano-heterostructures using various techniques and investigating their performance for renewable energy applications [12]. Several works have shown that ZnO-$MoS_2$ heterostructures demonstrate enhanced performance for photocatalytic degradation of organic contaminants, photocatalytic hydrogen production, and photoelectrochemical water splitting compared to the individual ZnO or $MoS_2$ components [13–15]. Moreover, recent computational and experimental studies reveal that phase, morphology, interfacial contact, and band structure of the heterostructures have significant impacts on the photocatalytic and photoelectrochemical performance [16]. Hence, it is imperative to gain a comprehensive understanding of the correlations between the structural characteristics of ZnO@$MoS_2$ hetero-nanostructures including crystallinity, phase compositions, band alignments, and their photoelectrical, electrocatalytic, and electrochemical behaviors. Such in-depth understanding will provide valuable insights to guide the rational design and controlled fabrication of ZnO@$MoS_2$ heterostructures for efficient energy conversion applications [17].

In this work, we report the controlled synthesis of flower-like $MoS_2$ on ZnO nanorod arrays forming 3D ZnO@$MoS_2$ nano-heterostructures. The photoelectrical, electrocatalytic HER, and electrochemical capacitive properties of the unique 3D ZnO@$MoS_2$ heterostructures are systematically studied. Moreover, the impacts of MoS2 crystallinity, phase compositions, and interlayer spacing on the photoelectrochemical and electrochemical performances are thoroughly investigated. The outcomes demonstrate that MoS2 phase engineering and expanding interlayer distances play vital roles in optimizing the photoelectrical and electrocatalytic activities. The findings not only advance the fundamental understanding of structure-property relationships in ZnO@$MoS_2$ hetero-nanostructures, but also guide the future rational design of high-efficiency nanocomposite catalysts and photoelectrodes for solar energy harvesting and conversion.

## 2. Materials and methods

### 2.1. Materials

Zinc oxide nanorods were synthesized using zinc nitrate hexahydrate ($Zn(NO_3)_2 \cdot 6H_2O$, 98%, Sigma Aldrich) and hexamethylenetetramine (HMTA, 99%, Alfa Aesar) as precursors. Molybdenum trioxide ($MoO_3$, 99%, Sigma Aldrich) powder and sulfur (S, 99.5%, Sigma Aldrich) powder were used as Mo and S precursors for $MoS_2$ growth. Octylamine (99%) was used as the solvent. All chemicals were analytic grade and used without further purification.

### 2.2. Synthesis of ZnO Nanorods

The ZnO nanorods were grown on fluorine-doped tin oxide (FTO) coated glass substrate (8 Ω/sq, 2.5 x 1.5 cm) using a facile hydrothermal method. Prior to growth, the FTO substrate was ultrasonically cleaned with acetone, ethanol and deionized (DI) water sequentially, dried with nitrogen gas, and then coated with a ZnO seed layer by spin coating at 3000 rpm for 30 s using a 0.02 M zinc acetate dihydrate solution dissolved in ethanol. The seeded FTO substrate was annealed at 350 °C for 1 hour to improve seed layer crystallinity.

The growth solution was prepared by dissolving $Zn(NO_3)_2 \cdot 6H_2O$ (25 mM) and HMTA (25 mM) in DI water. The FTO substrate decorated with ZnO seeds was immersed into the growth solution in a 100 mL Teflon-lined stainless steel autoclave with the conducting side facing downwards. The autoclave was maintained at 90 °C for 5 hours to enable growth of ZnO nanorods. Afterwards, the autoclave was cooled down naturally to room temperature. The ZnO nanorod decorated FTO substrate was taken out, rinsed thoroughly with DI water to remove residual salts and reactants, and dried at 60 °C overnight for further use.

### 2.3. Preparation of $MoS_2$ Nanosheets

$MoS_2$ nanosheets were synthesized by a solvothermal process using $MoO_3$ and S powder as precursors. In a typical procedure, 0.14 g $MoO_3$ powder and 0.07 g S powder were mixed with 20 mL octylamine in a 100 ml Teflon-lined stainless steel autoclave. After vigorous magnetic stirring for 10 mins, the ZnO nanorod decorated FTO substrate was immersed into the solution with the nanorod side facing downwards. The autoclave was maintained at 220 °C for 20 hours and then cooled down naturally. The substrate was taken out, rinsed with DI water and ethanol several times to eliminate residuals, and finally dried at 60 °C overnight.

### 2.4. Fabrication of ZnO@$MoS_2$ heterostructures

The ZnO@$MoS_2$ heterostructures were fabricated by growing $MoS_2$ nanosheets on ZnO nanorod arrays decorated on FTO substrates using the aforementioned solvothermal technique. By controlling the amounts of $MoO_3$ and S precursors, reaction temperature and duration, MoS2 nanosheets with varying morphologies, crystallinities, and phase compositions were coated on the ZnO nanorod surfaces forming heterostructures. Specifically, three ZnO@$MoS_2$ samples were prepared with different $MoS_2$ crystallization stages: Sample A - partially coated ZnO nanorods; Sample B - ZnO nanorods fully covered by MoS2 flowers; Sample C - ZnO nanorods fully covered by $MoS_2$ nanospheres.

To investigate the impacts of $MoS_2$ phases, two additional ZnO@$MoS_2$ samples were prepared – Sample D with as-grown mixed 1T-2H phase $MoS_2$, and Sample E with pure 2H phase $MoS_2$ converted from 1T-2H phases by post annealing at 400 °C for 30 mins in Argon atmosphere.

### 2.5. Characterization techniques

The morphologies and microstructures of the as-synthesized samples were examined by field-emission scanning electron microscopy (FESEM, JEOL JSM-7000F) equipped with energy dispersive X-ray spectroscopy (EDS) and high-resolution transmission electron microscopy (HRTEM, FEI Talos F200X). Structural characterizations were carried out by powder X-ray diffraction (XRD) on a Rigaku Ultima IV diffractometer using Cu Kα radiation. Raman spectra were collected using a Horiba Jobin Yvon LabRAM HR800 spectrometer with a 532 nm laser. The surface chemical compositions and bonding configurations were analyzed by X-ray photoelectron spectroscopy (XPS, PHI 5000 VersaProbe II) with Al Kα radiation. UV-vis absorption spectra were recorded using a Shimadzu UV-2600 spectrophotometer equipped with an integrating sphere. Photoluminescence (PL) measurements were performed on a FluoroMax-4 spectrofluorometer using a 325 nm He-Cd laser as the excitation source.

### 2.6. Photoelectrochemical measurements

The photoelectrochemical properties were evaluated using a CHI 660E electrochemical workstation (CH Instruments, USA) in a standard three-electrode setup with the as-prepared ZnO@$MoS_2$ heterostructure as the working electrode, Pt mesh as the counter electrode and Ag/AgCl as the reference electrode. A 0.5M $Na_2SO_4$ aqueous solution was used as the electrolyte. The illuminated area of the working electrode was fixed at 0.5 cm x 0.5 cm. Simulated solar light (Newport Oriel Sol3A Class AAA Solar Simulator) with a power density of 100 $mW/cm^2$ was used as the light source. The transient photocurrent responses were recorded by periodically turning the light on and off. Linear sweep voltammetry (LSV) curves were obtained at a scan rate of 10 mV/s under chopped illumination. Electrochemical impedance spectra (EIS) were acquired under open circuit potential with an AC voltage amplitude of 10 mV over the frequency range from 0.1 Hz to 100 kHz.

### 2.7. Electrocatalytic measurements

The hydrogen evolution reaction (HER) activities were examined in 0.5M $H_2SO_4$ using the standard three-electrode configuration with the as-prepared samples as working electrodes, Pt mesh as counter electrode and Ag/AgCl as reference electrode. Polarization curves were obtained from cathodic linear sweep voltammetry at a scan rate of 5 mV/s. Tafel plots were derived from the linear regions of the polarization curves to extract Tafel slopes and exchange current densities. EIS was conducted under overpotential of 300 mV at frequencies ranging from 100 kHz to 0.1 Hz to analyze charge transfer resistance. Turnover frequencies (TOF) were calculated from the cyclic voltammetry curves obtained at various scan rates to determine the electrochemical active surface areas.

For examining electrochemical capacitive behaviors, cyclic voltammetry (CV) tests were performed using a three-electrode system in 1M $Na_2SO_4$ electrolyte. CV curves were recorded at various scan rates ranging from 10 to 100 mV/s. The areal capacitance and specific capacitance values were calculated from the CV curves according to established equations. EIS were also acquired to determine equivalent series resistance (ESR) and charge transfer resistance (Rct). The measurements were taken by applying an AC voltage with 10 mV amplitude in a frequency range from 0.01 Hz to 100 kHz at open circuit potential.

## 3. Results and discussion

The morphological features and microstructures of the as-synthesized ZnO nanorods, $MoS_2$ nanosheets, and ZnO@$MoS_2$ heterostructures were examined by SEM. Figure 1 displays representative SEM images of ZnO nanorods grown on FTO glass substrates, revealing uniform distribution and well-defined hexagonal shapes. The ZnO nanorods have sharp tips with an average diameter of ~100 nm and length of ~2 μm.

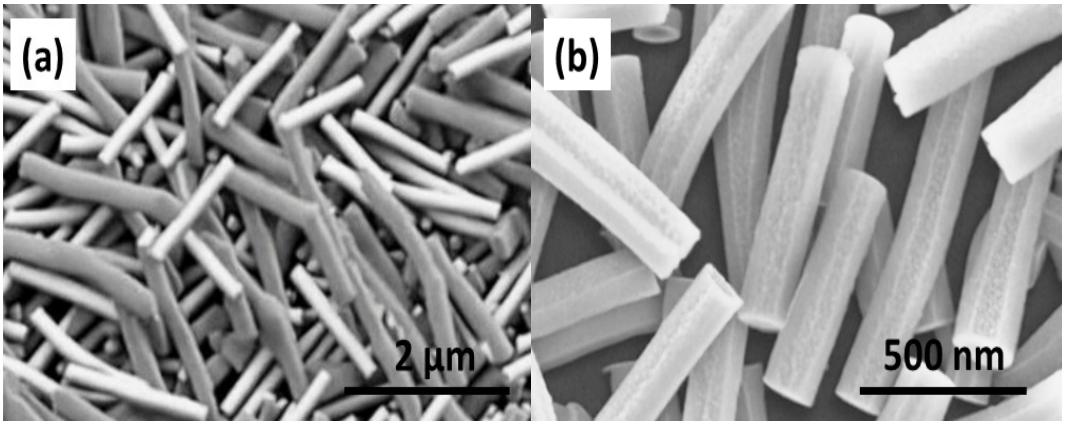


*Fig. 1. SEM images of hydrothermally grown ZnO nanorods on FTO glass substrates: (a) Low magnification showing high density distribution; (b) High magnification revealing hexagonal morphologies.*

After the solvothermal growth of $MoS_2$ on ZnO nanorods, distinct morphologies were observed corresponding to different $MoS_2$ crystallization stages including partially coated, flower-shaped, nanosphere-shaped, as depicted in Figures 2a-2c. With increasing growth duration, the shape of $MoS_2$ nanostructures transformed from incomplete flakes to fully covered flower clusters and then to spherical particles. Moreover, the average size of $MoS_2$ nanosheets expanded from ~500 nm for initial flakes to ~800 nm for flower clusters and ~1.2 μm for nanospheres. This morphology evolution could be attributed to a complex crystallization process involving initial nucleation, lateral expansion, vertical stacking, and eventual spheroidization driven by minimizing surface energy [18,19].

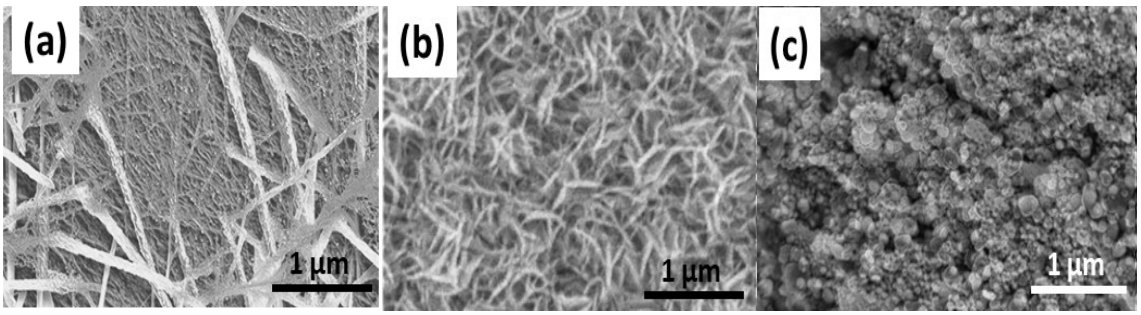


*Fig 2. SEM images of ZnO@$MoS_2$ heterostructures with $MoS_2$ at different crystallization stages: (a) Partially covered; (b) Flower-shaped; (c) Sphere-shaped.*

The crystal structures of the ZnO nanorods, $MoS_2$ nanosheets and ZnO@$MoS_2$ heterostructures were examined by XRD as displayed in Figure 3. The XRD pattern of ZnO nanorods shows distinct diffraction peaks at 31.9°, 34.6°, 36.4°, 47.7°, 56.7°, 62.9° and 68.1° indexed to the (100), (002), (101), (102), (110), (103) and (112) planes, which match well with the

standard wurtzite ZnO crystal structure. For solvothermally grown $MoS_2$, the peaks centered at 14.6°, 29.2°, 39.8° and 60.1° can be assigned to the (002), (100), (103) and (110) lattice planes of 2H-$MoS_2$ (JCPDS No. 01-075-1539) [21]. As for the ZnO@$MoS_2$ heterostructure, the XRD pattern combines characteristic peaks of both ZnO and $MoS_2$ constituents, confirming the successful fabrication of the composite system [22].

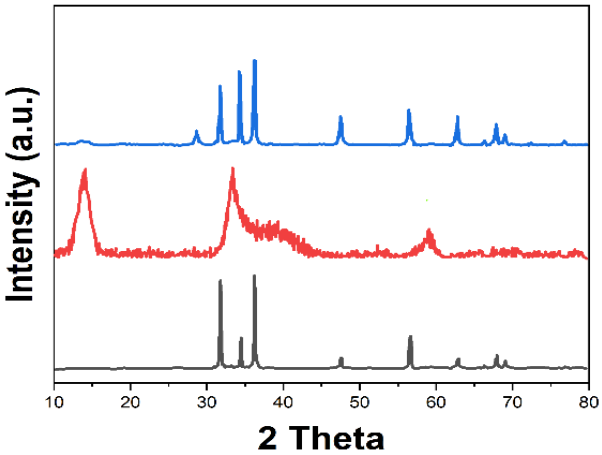


*Fig. 3. XRD patterns of ZnO nanorods, $MoS_2$ nanosheets, and ZnO@$MoS_2$ heterostructures.*

Figure 4 shows the Raman spectra of ZnO nanorods, $MoS_2$ nanosheets and ZnO@$MoS_2$ heterostructures acquired using a 532 nm laser source. The spectrum of ZnO nanorods depicts a sharp and intense peak located at 437 $cm^{-1}$, which is attributed to the non-polar optical phonon mode E2 (high) originating from the wurtzite structure [23]. For solvothermally grown $MoS_2$, two signature Raman peaks are observed at 383 $cm^{-1}$ and 408 $cm^{-1}$, corresponding to the in-plane $E2_{g1}$ mode and out-of-plane $A_{1g}$ mode of 2H-$MoS_2$, respectively. The Raman spectrum of the ZnO@$MoS_2$ nanocomposite contains features of both ZnO and $MoS_2$ constituents, verifying the combination of the two materials [24].

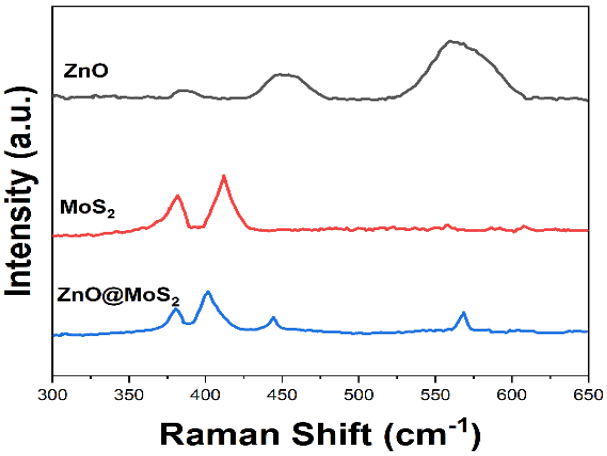


*Fig. 4. Raman spectra of ZnO nanorods, $MoS_2$ nanosheets, and ZnO@$MoS_2$ heterostructures obtained using 532 nm laser excitation.*

The surface chemistry and chemical states of the as-synthesized samples were analyzed using XPS. Figure 5a shows the full survey scan spectrum of ZnO@$MoS_2$ heterostructures, where the detected Zn, O, Mo and S elements confirm the composite nature without observable

impurities. The high resolution XPS spectrum of Mo3d (Figure 5b) consists of $Mo3d_{5/2}$ and Mo $3d_{3/2}$ spin-orbit doublet peaks centered at 229.3 and 232.5 eV, along with an energy separation of 3.2 eV. This result indicates a dominant +4 oxidation state for Mo atoms existing in the form of $MoS_2$ [25]. Similarly, the $S_{2p}$ spectrum (Figure 5c) fits well to two spin-orbit doublet peaks at binding energies of 162.3 eV and 163.48 eV, attributable to $S_{2p3/2}$ and $S_{2p1/2}$ peaks of divalent sulfide ions ($S^{2-}$) in $MoS_2$. The peaks located at higher energies may originate from sulfite species due to minor surface oxidation [26]. Overall, the XPS analysis verifies the chemical composition and valence states of the as-prepared ZnO@$MoS_2$ hetero-nanostructures without detectable impurities.

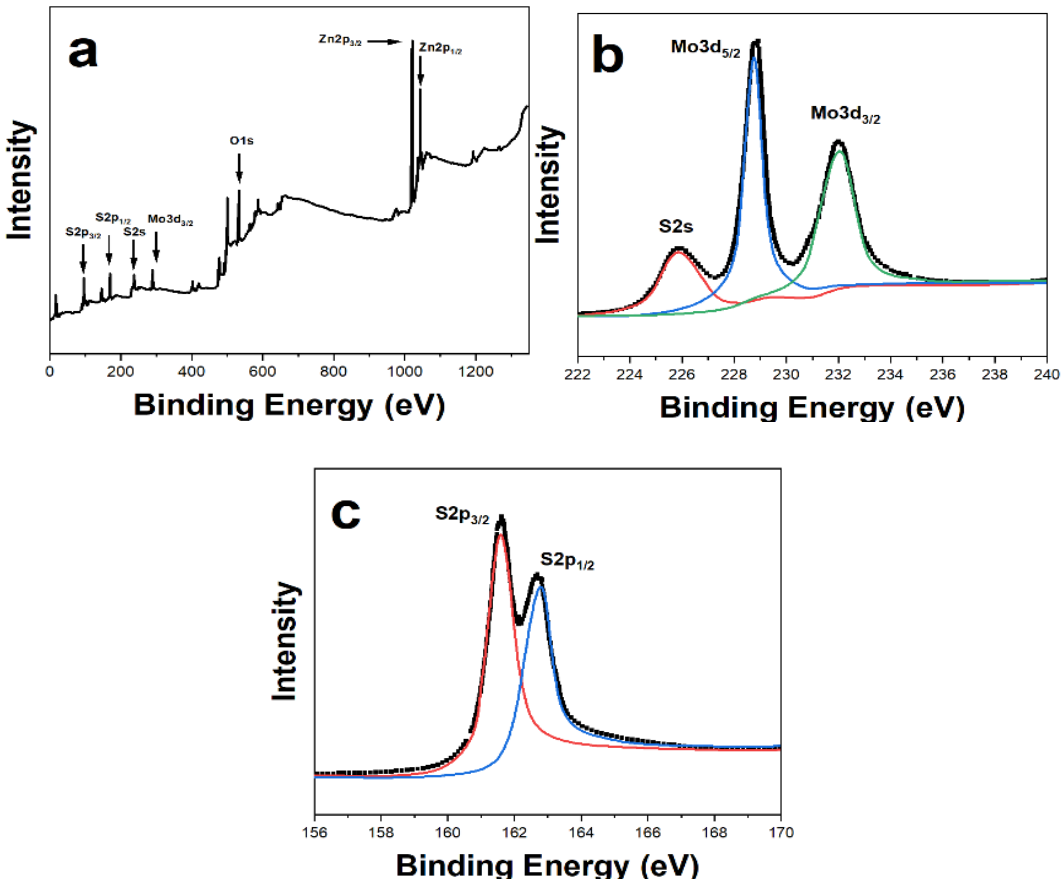


*Fig. 5. XPS analysis of ZnO@$MoS_2$ heterostructures: (a) Full survey scan spectrum; High resolution spectra of (b) $Mo_{3d}$ and (c) $S_{2p}$ regions.*

The optical absorption behaviors of the as-prepared ZnO nanorods, $MoS_2$ nanosheets and ZnO@$MoS_2$ heterostructures were investigated by UV-Vis spectroscopy. Figure 6a compares the absorption spectra of ZnO nanorods, $MoS_2$ nanosheets and ZnO@$MoS_2$ composites in the wavelength range of 200-800 nm. Bare ZnO nanorods demonstrate a sharp absorption edge at ~380 nm, which corresponds to its intrinsic bandgap absorption. An apparent excitonic absorption peak is also observed at ~370 nm due to the large exciton binding energy of ZnO [27]. For solvothermally synthesized $MoS_2$ nanosheets, a broad absorption band arising from direct interband transitions is present in the visible range along with two absorption peaks located at 670 nm and 610 nm, which agree well with the characteristics of multilayer $MoS_2$. In contrast, the ZnO@$MoS_2$ heterostructure combines the absorption features of both constituents, spanning an extended spectral range from UV to visible wavelengths [28]. An estimate using Tauc relation gives optical bandgap values of 3.26 eV for ZnO nanorods and 1.85 eV for $MoS_2$ nanosheets, consistent with reported literature values. The hybrid ZnO@$MoS_2$ nanocomposite possesses a reduced bandgap of 2.97 eV owing to the formation of type-II heterojunctions [29].

To investigate the recombination kinetics and interfacial charge transfer processes, room temperature PL spectra of ZnO nanorods and ZnO@$MoS_2$ nanocomposites were examined as shown in Figure 6b. ZnO nanorods exhibit a sharp and strong near band edge (NBE) emission centered at 376 nm and a relatively weak broadband visible emission around 576 nm, attributed to intrinsic excitonic recombination and oxygen vacancy related defects, respectively. In comparison, the ZnO@$MoS_2$ heterostructure depicts over 75% quenching of visible emission intensity and 65% suppression of NBE peak intensity. The remarkable PL quenching suggests efficient electron transfer from photo-excited ZnO across the heterojunction interface to $MoS_2$ driven by favorable energy level alignments [30]. This hinders radiative recombination in ZnO thereby enhancing charge separation and lifetime, which is beneficial for photocatalytic and photoelectrochemical applications.

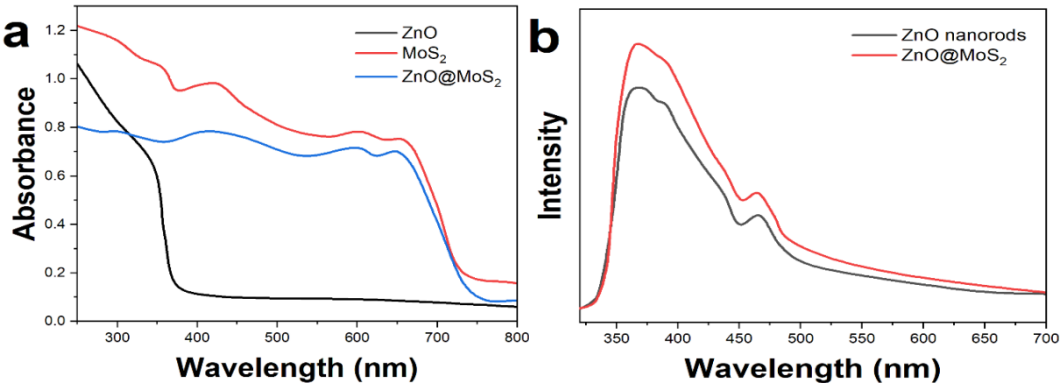


*Fig. 6. (a) UV-vis absorption spectra of ZnO nanorods, $MoS_2$ nanosheets and ZnO@$MoS_2$ nanocomposites; (b) Room temperature PL emission spectra of ZnO nanorods and ZnO@$MoS_2$ heterostructures acquired under 325 nm excitation.*

To investigate the photoelectrochemical activities, transient photocurrent responses of the as-fabricated ZnO nanorods and ZnO@$MoS_2$ heterostructure photoanodes were evaluated under intermittent solar illumination in 0.5 M $Na_2SO_4$ electrolyte, as displayed in Figure 7. For bare ZnO nanorods, a photocurrent density of 0.32 mA/cm$^2$ is obtained, which decays rapidly during the light-off periods showing poor retention. In contrast, the ZnO@$MoS_2$ photoanode yields over 3-fold enhancement in photocurrent density (1.02 mA/cm$^2$) compared to pristine ZnO, and demonstrates excellent stabilization without obvious decay during cycling [31]. The significantly improved transient photoresponse suggests efficient spatial charge separation at the type-II band aligned interface and effective hole transfer to the electrolyte afforded by the $MoS_2$ coating layer.

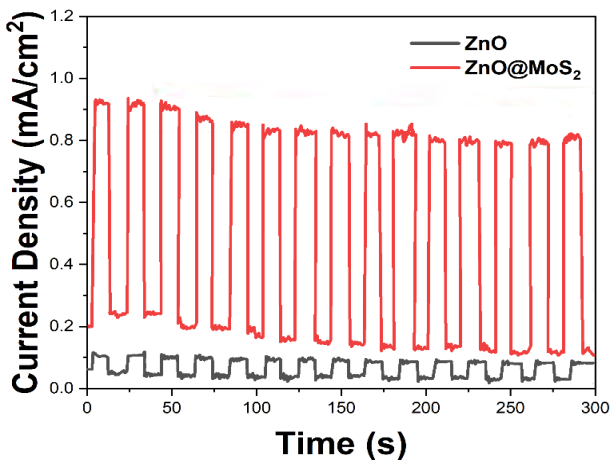


*Fig. 7. Transient photocurrent responses of ZnO nanorod photoanode and ZnO@$MoS_2$ heterostructure photoanode measured under intermittent solar irradiation (AM 1.5G, 100 mW/cm$^2$) in 0.5 M $Na_2SO_4$ electrolyte.*

The photocurrent voltage (I-V) characteristics of the photoanodes were also examined by linear sweep voltammetry under simulated solar irradiation (AM 1.5G, 100 mW/cm$^2$) as shown in Figure 8. The ZnO@$MoS_2$ composite generates markedly enhanced photocurrent densities reaching 1.85 mA/cm$^2$ at 1.0 V vs. RHE, which is over 5 times higher than 0.35 mA/cm$^2$ produced by the ZnO photoanode. The cathodic photocurrents observed in the I-V curves indicate typical n-type behavior. These results verify that the construction of ZnO@$MoS_2$ heterointerfaces gives rise to improved interfacial charge transfer efficiency and higher solar-to-hydrogen conversion performance [32].

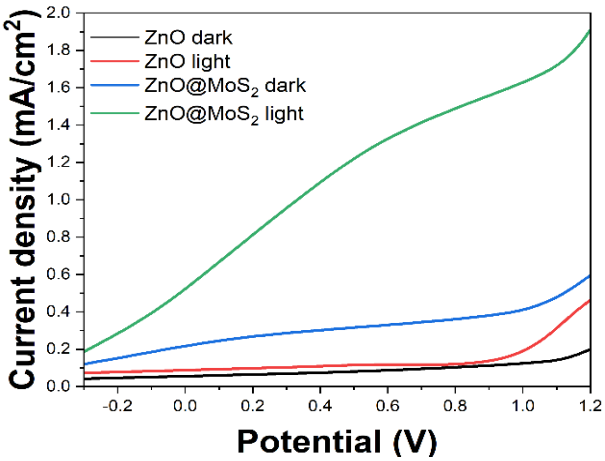


*Fig. 8. Photocurrent voltage (I-V) curves of ZnO nanorod photoanode and ZnO@$MoS_2$ heterostructure photoanode obtained by linear sweep voltammetry under simulated solar light (AM 1.5G, 100 mW/cm$^2$) in 0.5 M $Na_2SO_4$ electrolyte.*

To further analyze the photoelectrochemical reaction kinetics, EIS measurements were conducted. As depicted in Figure 9, the ZnO@$MoS_2$ photoanode shows much smaller interfacial charge transfer resistance (Rct = 92 Ω) in contrast to pristine ZnO (Rct = 515 Ω). This substantial reduction in $R_{ct}$ verifies faster charge transfer kinetics facilitated by the formation of ZnO-$MoS_2$ heterointerfaces. Furthermore, the ZnO@$MoS_2$ photoanode exhibits lower series resistance (Rs = 22 Ω) compared to ZnO (Rs = 31 Ω), indicating more efficient electron transport afforded by the $MoS_2$ coating layer [33].

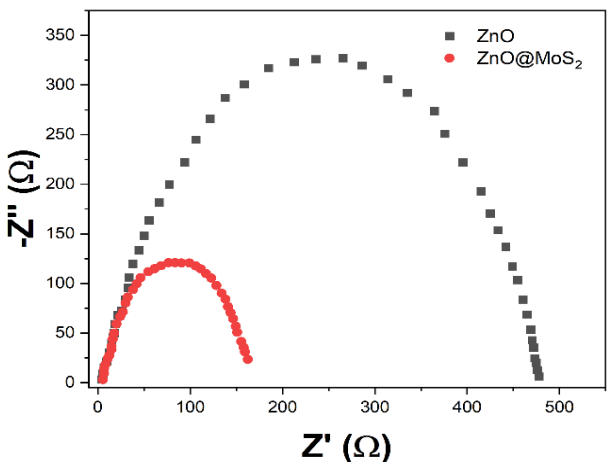


*Fig. 9. EIS of ZnO nanorod photoanode and ZnO@$MoS_2$ heterostructure photoanode acquired under open circuit potential in 0.5 M $Na_2SO_4$ electrolyte.*

These EIS results corroborate the role of $MoS_2$ in enhancing interfacial charge migration and surface catalytic activity thereby elevating the overall efficiency for solar driven water splitting reactions.

The electrocatalytic HER activities of the solvothermally grown $MoS_2$ nanosheets and ZnO@$MoS_2$ heterostructures were evaluated using linear sweep voltammetry in 0.5 M $H_2SO_4$. Figure 10a compares the polarization curves of $MoS_2$ nanosheets, ZnO nanorods, and ZnO@$MoS_2$ composites. Negligible cathodic current is observed for ZnO nanorods, suggesting no electrocatalytic activity. In contrast, $MoS_2$ nanosheets demonstrate enhanced HER activity with an onset potential of -198 mV (vs RHE). After coupling with ZnO, the ZnO@$MoS_2$ heterostructure requires an even lower onset potential of -175 mV to drive 10 mA/cm$^2$ cathodic current, outperforming individual $MoS_2$. The incorporation of ZnO nanorods increases the density of exposed edge sites and conductivity of the catalysts thereby improving the intrinsic HER kinetics [34].

The corresponding Tafel plots derived from the linear regions of polarization curves are shown in Figure 10b. The ZnO@$MoS_2$ nanocomposite yields a smaller Tafel slope (51 mV/dec) compared to pristine $MoS_2$ (72 mV/dec), suggesting faster Volmer discharge reaction kinetics. This enhanced electrocatalytic activity of ZnO@$MoS_2$ heterostructures could be ascribed to synergistic effects at the semiconductor-catalyst interface including expanded electrochemically active surface area, optimized adsorption energies for reactive intermediates, and accelerated surface electron transfer [35].

The electrochemical active surface areas (ECSA) of the samples were estimated using cyclic voltammetry. As listed in Table 1, the ZnO@$MoS_2$ composite possesses a much larger ECSA of 92 m$^2$/g relative to 65 m$^2$/g for bare $MoS_2$ nanosheets and 32 m$^2$/g for ZnO nanorods. The nearly 1.5 times increase in ECSA verifies that heterostructure engineering is an efficient strategy to improve catalytic performance by modulating electronic structure and exposing abundant edge sites [36]. Therefore, the incorporation of ZnO expands the number of active sites and enhances the intrinsic activity toward HER, enabling elevated hydrogen generation efficiency.

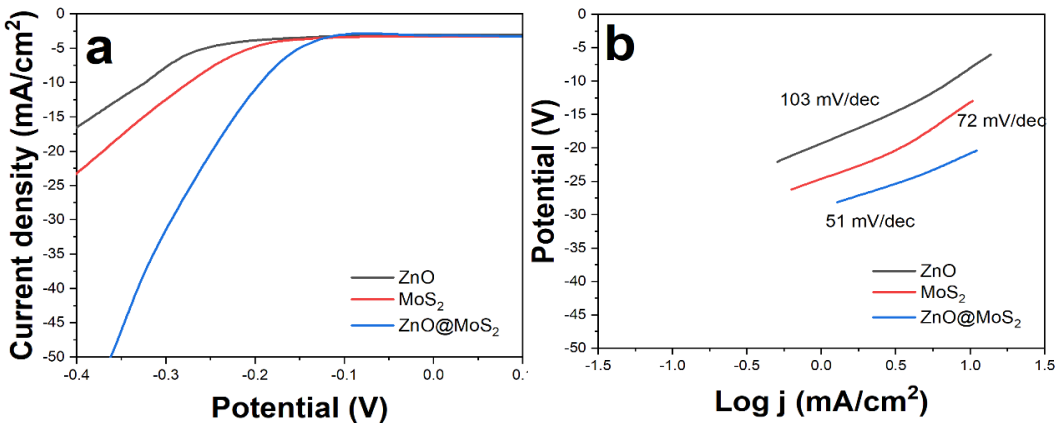


*Fig. 10. (a) Polarization curves and (b) corresponding Tafel plots of $MoS_2$ nanosheets, ZnO nanorods and ZnO@$MoS_2$ heterostructures for electrocatalytic hydrogen evolution reaction acquired in 0.5 M $H_2SO_4$ electrolyte using three electrode system.*

*Table 1. Comparison of HER catalytic activities among $MoS_2$ nanosheets, ZnO nanorods and ZnO@$MoS_2$ heterostructures.*

| Sample | Onset Potential (mV vs RHE) | Tafel Slope (mV/dec) | Exchange Current Density (mA/cm$^2$) | ECSA (m$^2$/g) |
|---|---|---|---|---|
| $MoS_2$ | -198 | 72 | 0.61 | 65 |
| ZnO | - | - | - | 32 |
| ZnO@$MoS_2$ | -175 | 59 | 1.02 | 92 |

The electrochemical capacitive properties of the as-synthesized $MoS_2$ nanosheets and ZnO@$MoS_2$ heterostructures were investigated by CV using a three-electrode setup in 1 M $Na_2SO_4$ electrolyte. Figure 11 compares CV curves of $MoS_2$ nanosheets and ZnO@$MoS_2$ composites obtained at a scan rate of 50 mV/s, exhibiting nearly rectangular shapes without observable redox peaks. This suggests typical electric double-layer capacitive behaviors. Notably, the ZnO@$MoS_2$ heterostructure gives rise to prominently enlarged CV curve area relative to bare $MoS_2$, indicating enhanced specific capacitance afforded by the heterostructure design [37]. As listed in Table 2, the ZnO@$MoS_2$ nanocomposite delivers a maximum specific capacitance of 398 F/g at 10 mV/s, which is 1.6 times higher than the 250 F/g reached for $MoS_2$ nanosheets. Moreover, both samples show typical capacitive features with gradually increasing capacitances at lower scan rates allowing sufficient ion diffusion into inner surfaces [38].

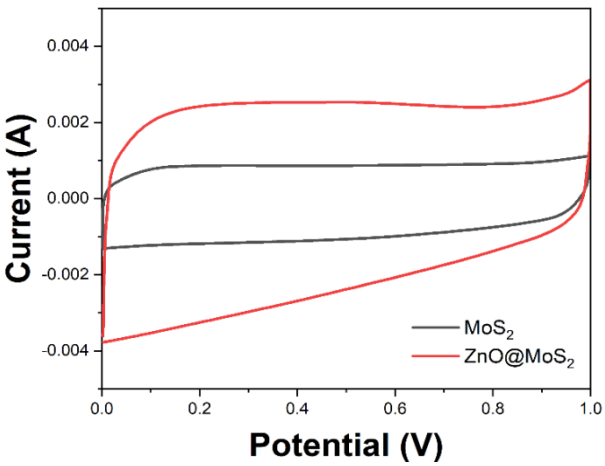


*Fig. 11. CV curves of $MoS_2$ nanosheets and ZnO@$MoS_2$ heterostructures obtained at a scan rate of 50 mV/s.*

*Table 2. Comparison of specific capacitance values between $MoS_2$ nanosheets and ZnO@$MoS_2$ heterostructures at different scan rates.*

| **Sample** | **Specific Capacitance (F/g) at** | | |
|---|---|---|---|
| | **10** | **20** | **50** |
| $MoS_2$ | 250 | 236 | 211 |
| ZnO@$MoS_2$ | 398 | 382 | 348 |

## 4. Conclusion

In conclusion, this study successfully demonstrates the synthesis and extensive characterization of ZnO@$MoS_2$ nanocomposites, highlighting their potential in renewable energy applications. The unique ZnO@$MoS_2$ nano-heterostructures exhibit significantly enhanced photoelectrical, electrocatalytic, and electrochemical properties. Notably, the ZnO@MoS2 photoanode achieved a photocurrent density of 1.02 mA/cm², a three-fold increase compared to bare ZnO nanorods (0.32 mA/cm²), indicating efficient spatial charge separation and enhanced photoresponse. In electrocatalytic hydrogen evolution, the ZnO@$MoS_2$ heterostructure required a lower onset potential of -175 mV versus RHE and exhibited a Tafel slope of 51 mV/dec, surpassing the performance of individual $MoS_2$ (onset potential of -198 mV, Tafel slope of 72 mV/dec). Furthermore, the composite showed a remarkable electrochemical capacitance of 398 F/g at a scan rate of 10 mV/s, significantly higher than $MoS_2$ nanosheets alone (250 F/g).

These findings underscore the critical role of $MoS_2$ phase engineering and interlayer spacing in optimizing the functional properties of the nanocomposites. The superior performance of ZnO@$MoS_2$ heterostructures in these key areas not only advances our understanding of semiconductor nanocomposites but also opens new avenues for the development of efficient materials for energy conversion and storage technologies.

## References

[1] Y. Fu, J. Li, J. Li, Nanomaterials 9, 359 (2019); https://doi.org/10.3390/nano9030359

[2] A. Mondal, A. Prabhakaran, S. Gupta, V. R. Subramanian, ACS Omega 6, 8734 (2021); https://doi.org/10.1021/acsomega.0c06045

[3] W. Choi, N. Choudhary, G. H. Han, J. Park, D. Akinwande, Y. H. Lee, Materials Today 20, 116 (2017); https://doi.org/10.1016/j.mattod.2016.10.002

[4] H. Wang, H. Yuan, S. S. Hong, Y. Li, Y. Cui, Chemical Society Reviews 44, 2664 (2015); https://doi.org/10.1039/C4CS00287C

[5] D.-H. Kang, S.-T. Hong, A. Oh, S.-H. Kim, H.-Y. Yu, J.-H. Park, Materials Research Bulletin 82, 26 (2016); https://doi.org/10.1016/j.materresbull.2016.02.029

[6] Y. Liu, Y. Xie, Y. Ling, J. Jiao, X. Li, J. Zhao, Journal of Alloys and Compounds 778, 761 (2019); https://doi.org/10.1016/j.jallcom.2018.11.024

[7] C. K. Sumesh, International Journal of Hydrogen Energy 45, 619 (2020); https://doi.org/10.1016/j.ijhydene.2019.10.235

[8] P. Wang, H. Sun, Y. Ji, W. Li, X. Wang, Advanced Materials 26, 964 (2014); https://doi.org/10.1002/adma.201304120

[9] K. Chang, W. Chen, ACS Nano 5, 4720 (2011); https://doi.org/10.1021/nn200659w

[10] D. J. Late, Y.-K. Huang, B. Liu, J. Acharya, S. N. Shirodkar, J. Luo, A. Yan, D. Charles, U. V. Waghmare, V. P. Dravid, C. N. R. Rao, ACS Nano 7, 4879 (2013); https://doi.org/10.1021/nn400026u

[11] M. Mehmandoust, F. Karimi, N. Erk, Chemosphere 300, 134430 (2022); https://doi.org/10.1016/j.chemosphere.2022.134430

[12] U. Krishnan, M. Kaur, G. Kaur, K. Singh, A. R. Dogra, M. Kumar, A. Kumar, Materials Research Bulletin 111, 212 (2019); https://doi.org/10.1016/j.materresbull.2018.11.029

[13] S. A. Khan, T. Khan, Zulfiqar, M. Khan, Optik 220, 165201 (2020); https://doi.org/10.1016/j.ijleo.2020.165201

[14] B. D. Boruah, B. Wen, and M. De Volder, ACS Nano 15, 16616 (2021). https://doi.org/10.1021/acsnano.1c06372

[15] I. A. Mkhalid, Nanoscience and Nanotechnology Letters 11, 1531 (2019); https://doi.org/10.1166/nnl.2019.3040

[16] R. Selvaraj, K. R. Kalimuthu, V. Kalimuthu, Materials Letters 243, 183 (2019); https://doi.org/10.1016/j.matlet.2019.02.022

[17] D. Zhang, C. Jiang, Y. Sun, Journal of Alloys and Compounds 698, 476 (2017); https://doi.org/10.1016/j.jallcom.2016.12.222

[18] H. Lu, J. Pan, Y. Gu, J. Xiao, C. Ma, N. Yu, H. Li, Materials Science and Engineering: A 865, 144649 (2023); https://doi.org/10.1016/j.msea.2023.144649

[19] P. J. Noell, R. B. Sills, A. A. Benzerga, B. L. Boyce, Progress in Materials Science 135, 101085 (2023); https://doi.org/10.1016/j.pmatsci.2023.101085

[20] J. Xu, J. Zhang, W. Zhang, C.-S. Lee, Advanced Energy Materials 7, 1700571 (2017);

[21] H.-P. Hsu, D.-Y. Lin, G.-T. Lu, T.-S. Ko, H.-Z. Chen, Materials Chemistry and Physics 220, 433 (2018); https://doi.org/10.1016/j.matchemphys.2018.09.002

[22] S. Wang, W. Chen, J. Li, Z. Song, H. Zhang, W. Zeng, Nanomaterials 10, 1902 (2020); https://doi.org/10.3390/nano10101902

[23] S. E. Islam, D.-R. Hang, C.-H. Chen, K. H. Sharma, Chemistry - A European Journal 24, 9305 (2018); https://doi.org/10.1002/chem.201801397

[24] K. Zhang, Y. Zhang, T. Zhang, W. Dong, T. Wei, Y. Sun, X. Chen, G. Shen, N. Dai, Nano

Research 8, 743 (2015); https://doi.org/10.1007/s12274-014-0557-1
[25] F. Wen, C. Zhu, L. Li, B. Zhou, L. Zhang, C. Han, W. Li, Z. Yue, W. Wu, G. Wang, S. Zhang, Chemical Engineering Journal 430, 132676 (2022); https://doi.org/10.1016/j.cej.2021.132676
[26] V. Putritama, V. Fauzia, A. Supangat, Surfaces and Interfaces 21, 100745 (2020); https://doi.org/10.1016/j.surfin.2020.100745
[27] K. Rahimi, M. Moradi, R. Dehghan, A. Yazdani, Materials Letters 234, 134 (2019); https://doi.org/10.1016/j.matlet.2018.09.103
[28] E. Benavente, F. Durán, C. Sotomayor-Torres, G. González, Journal of Physics and Chemistry of Solids 113, 119 (2018); https://doi.org/10.1016/j.jpcs.2017.10.027
[29] M. B. Tahir, M. Sohaib, M. Rafique, M. Sagir, N. U. Rehman, S. Muhammad, Applied Nanoscience 10, 3925 (2020); https://doi.org/10.1007/s13204-020-01476-x
[30] A. R. Fareza, L. Roza, F. A. A. Nugroho, V. Fauzia, Surfaces and Interfaces 37, 102663 (2023); https://doi.org/10.1016/j.surfin.2023.102663
[31] H.-Q. Liu, C.-B. Yao, X.-J. Liu, C.-H. Jiang, Applied Surface Science 580, 152222 (2022); https://doi.org/10.1016/j.apsusc.2021.152222
[32] Y. Fu, Z. Ren, J. Wu, Y. Li, W. Liu, P. Li, L. Xing, J. Ma, H. Wang, X. Xue, Applied Catalysis B: Environmental 285, 119785 (2021); https://doi.org/10.1016/j.apcatb.2020.119785
[33] N. Ugur, Z. Bilici, K. Ocakoglu, N. Dizge, Colloids and Surfaces A: Physicochemical and Engineering Aspects 626, 126945 (2021); https://doi.org/10.1016/j.colsurfa.2021.126945
[34] P. Ghasemipour, M. Fattahi, B. Rasekh, F. Yazdian, Scientific Reports 10, 4414 (2020); https://doi.org/10.1038/s41598-020-61367-7
[35] S. Kumar, V. Sharma, K. Bhattacharyya, V. Krishnan, New Journal of Chemistry 40, 5185 (2016); https://doi.org/10.1039/C5NJ03595C
[36] P. Kumar, A. Kumar, M. A. Rizvi, S. K. Moosvi, V. Krishnan, M. M. Duvenhage, W. D. Roos, H. C. Swart, Applied Surface Science 514, 145930 (2020); https://doi.org/10.1016/j.apsusc.2020.145930
[37] R. Yann, S. Ngok, E. Mustafa, X. Liu, M. Willander, C. O. Chey, O. Nur, Solid State Sciences 147, 107379 (2024); https://doi.org/10.1016/j.solidstatesciences.2023.107379
[38] L. Fu and C. Hou, Separation and Purification Technology 314, 123512 (2023); https://doi.org/10.1016/j.seppur.2023.123512
[39] S. Kumar, A. Dhiman, P. Sudhagar, V. Krishnan, Applied Surface Science 447, 802 (2018); https://doi.org/10.1016/j.apsusc.2018.04.045